Conservative implementation of the interface sharpening equation within an incompressible isothermal multifield approach

Solène Fleau[*,**,1], Stéphane Mimouni[*,2], Stéphane Vincent[**,3]

[*]Electricité de France, R&D Division, 6 Quai Watier, Chatou, France.

[**]Université Paris-Est Marne-La-Vallée, UMR CNRS 8208, Laboratoire de Modélisations et Simulation Multi-Echelle, 5 boulevard Descartes, Champs sur Marne, 77454 Marne-la-Vallée Cedex 2, France.

[1]Email: solene.fleau@edf.fr

[2]Corresponding author. Email: stephane.mimouni@edf.fr, [3]Email: stephane.vincent@u-pem.fr

Abstract Bubbly flows occurring in nuclear power plants remain a major limiting phenomenon for the analysis of operation and safety. Therefore, the choice was made to investigate these complex flows with a multifield approach, considering the gas phase as two separated fields. In so doing, the small and spherical bubbles are considered as parts of the dispersed field whereas the distorted bubbles are simulated with an interface locating method. The flow motion is followed using the two-fluid model of Ishii [1975, *Thermo-fluid dynamic, theory of two-phase flow*, Eyrolles] extended to n-phases. Nevertheless, this model is known to spread numerically large interfaces, which results in a poor accuracy in the calculation of the local flow parameters such as curvature. Therefore, this paper is focused on the accurate simulation of the large scale interfaces. The implementation of an artificial interface sharpening equation is detailed to limit the interface smearing. The activation criteria are also described. Special attention is given to mass conservation. All these steps are illustrated with test cases of isothermal, incompressible and laminar separated two-phase flows. A final validation is proposed with the simulation of the Bhaga's rising bubble problem [Bhaga, D.

and Weber, M.E., 1981, Bubbles in viscous liquids: shape, wakes and velocities, *J. of Fluid Mech*., Vol. 105, pp. 61-85] and the Kelvin-Helmhotz instability in the Thorpe's experiment configuration [Thorpe, S., 1969, Experiments on the instability of stratified shear flows: immiscible fluids, *J. Fluid Mech.*, Vol. 39, pp 25-48].

Keywords: Multiphase flows, Computational multi-fluid dynamics, Multifield approach, Large interfacial structures, Interface sharpening equation

Highlights:

- A special treatment including capillary forces is proposed to resolve large interfaces within a multifield approach using a computational multi-fluid dynamics code based on a finite volume discretization.
- An interface sharpening equation is implemented and adapted to the two-fluid formulation.
- The large interface locating approach is validated with a large range of isothermal, incompressible and laminar test cases from bubbly flows to interfacial liquid/liquid test cases, including convergence studies.

Nomenclature

Roman letters:		
a	-	Major axis of an ellipse
D	m	Bubble diameter
D_{diff}	$m^{-2}.s^{-1}$	Diffusion coefficient
g	$m.s^{-2}$	Gravitational constant
I	$kg.m^{-2}.s^{-2}$	Interfacial momentum transfer
k	m^{-1}	Wavenumber
n	-	Unit interface normal vector
P	Pa	Pressure
R	m	Bubble radius
S	s^{-1}	Viscous stress tensor
u	$m.s^{-1}$	Velocity
U	$m.s^{-1}$	Average interface velocity

Subscripts and superscripts:	
*	Intermediate values
int	Interface
i	Space direction
I, J	Cell index
k	Field index
n, n+1	Time step number
$ncel$	Total number of cells

Greek letters:		
θ, γ	-	Angular coordinates
ξ	-	Convergence order
Δx	m	Cube root of the cell volume
ρ_k	$kg.m^{-3}$	Density of field k
μ_k	Pa.s	Dynamic viscosity of field k
κ	m^{-1}	Interface curvature
Γ	$kg.m^{-3}.s^{-1}$	Interfacial mass transfer
ω	s^{-1}	Pulsation
σ	$N.m^{-1}$	Surface tension coefficient
β	-	Threshold coefficient
Δt	s	Time step
Ω	m^3	Volume element
α_k	-	Volume fraction of field k
τ	s	Characteristic time scale

1. Introduction

In nuclear power plants with pressurized water reactor or boiling water reactor, the steam generator integrity is crucial to prevent radiological exposures. Therefore, investigations have been carried out to predict the properties of the flow in terms of flow types and bubble sizes [Hao *et al.* 2014, Ma *et al.* 2014, Wang *et al.* 2012 and Watanabe *et al.* 2014]. Nevertheless, the variety of flow regimes (annular flow, dispersed bubbles and droplets, large and deformable bubbles) existing in vertical superheated tubes makes the simulations really challenging.

These complex flows have interested many research groups, which have developed and validated methods to track accurately interfaces. Thus, significant results have been obtained on turbulent deformable interfaces including mass and heat transfers with the Volume Of

Fluid (VOF) approach [Borniaa *et al.* 2011], the level set method [Di Bari *et al.* 2013] and the front tracking method [Dabiri and Tryggvason 2015]. Nevertheless, to be accurate, these methods require tracking all interfacial scales. For industrial applications, where the computational domain can have lengths in the order of a few meters, more than billion cells should be necessary to precisely simulate bubbles of less than a millimeter. However, such mesh refinements reach the current computational limit.

To deal with such flows, different approaches have been developed. A first one consists in simulating accurately the larger scales using interface tracking methods described above and considering the badly resolved structures as dispersed particles followed in a Lagrangian manner. This approach has been implemented by several research groups with the level set method [Capecelatro *et al.* 2010 and Herrmann 2010] and with the VOF method [Tomar *et al.* 2010 and Ling *et al.* 2015]. A second approach, called the multifield approach, has been first introduced a long time ago by Anderson and Jackson [1967] and Drew and Lahey [1979]. It is explored in this article. Contrary to the first method, the multifield approach is based on a two-fluid model initially used to simulate complex flows containing a continuous phase and small spherical inclusions modeled through a dispersed approach. Nevertheless, the dispersed model allows following only inclusions with a spherical shape with sizes smaller than the grid cell under a scale separation asumption. Thus, the idea of the multifield approach proposed in this paper is to extend the two-fluid model for the simulation of large and deformable inclusions. For this purpose, a notion of "field" is introduced. In a water/steam flow for example, three fields for two phases are considered: a dispersed field representing the small spherical bubbles, a continuous water field and a continuous steam field [Denèfle *et al.* 2015]. Thus, in each grid cell, one velocity and one volume fraction per field are defined. The two-fluid model equations are solved for each field in the whole domain. The large bubbles are then defined by interfaces between the continuous water field and the continuous steam field

containing the large bubble. This method can be applied to various types of inclusions: droplets or bubbles. Thus, it is important to note that the way of locating interfaces is totally different from the methods presented above, which consider one set of parameters (viscosity, density and velocity) in the whole domain and which follows interfaces by solving advection equations of Eulerian characteristic functions. To follow the dispersed field, some research groups have worked on Lagrangian methods [Zuzio *et al.* 2013] and on Eulerian methods [Vallet and Borghi 1999 and Lebas *et al.* 2009]. Here, the choice has been made to use an Eulerian approach. The models for the interfacial transfers related to this dispersed field have been well studied and validated [Mimouni *et al.* 2011]. The modeling effort is then currently focused on the large interfaces formed by two continuous fields. This article is devoted to the simulation of these interfaces in isothermal incompressible and laminar flows. Within the multifield approach, an accurate interface location method is required to evaluate precisely the local quantities such as surface tension forces, interfacial normal vectors or curvatures and to predict the evolution of these large scale interfacial structures. Nevertheless, the two-fluid model is known to numerically spread large interfaces [Štrubelj 2009 and Zuzio *et al.* 2013].

Thus, different methods have been developed to prevent the interface smearing. A first idea has been proposed by Saurel and Abgrall [1999] and is based on the resolution of an extra equation for the volume fractions. This method allows simulating accurately highly compressible flows and strong shock waves. Then, Xiao *et al.* [2005] presented a hyperbolic tangent interpolation of the volume fraction at each time step. The tangent of hyperbola interface capturing (THINC) method has been applied to simulations within a VOF method and showed significant improvements of the interface location [Xiao *et al.* 2005, Xiao *et al.* 2011 and Ii *et al.* 2011]. This method has been adapted to the two-fluid model [Nonomura *et al.* 2014] for the simulation of compressible flows. More recently, another interface sharpening technique has been developed, based on the resolution of an anti-diffusion

equation. Good results have also been obtained with a two-fluid modeling [So *et al.* 2011]. Finally, Hänsch *et al.* [2012] proposed to add a clustering force in the momentum balance equation. This method avoids solving an extra equation and has been validated for the simulation of three field two-fluid test cases.

In the present paper, a third interface sharpening method has been implemented, suitable for the simulation of incompressible flows with structured or unstructured grids, which are in the scope of this work. The technique, initially proposed by Olsson and Kreiss [2005] for the level set method, involves the resolution of a compression equation. The method has also been successfully applied to a two-fluid model [Štrubelj 2009, Denèfle *et al.* 2015].

Our study will be focused on the large scale interfaces within the multifield approach in isothermal and incompressible conditions. The implementation of a modified interface sharpening equation initially developed by Olsson and Kreiss [2005] will be detailed to limit the interface smearing. The different choices to adapt the method to a two-fluid model will be illustrated with the simulation of different separated two-phase flows. Thus, we will take special care of the mass fluxes defined in the compression equation to ensure mass conservation. Moreover, two criteria will be defined to activate the sharpening equation only when the large interfaces are spread.

The first part of this article is devoted to the computational framework developed for the multifield approach. Then, the numerical schemes of the Computational Fluid Dynamics (CFD) tool are briefly described to highlight the effect of the implementation of the interface sharpening equation. Different crucial parameters of this implementation are then discussed with examples of their effects on simulations of two-phase flows. Finally, Bhaga's rising bubbles [Bhaga and Weber 1981] and Kelvin-Helmholtz instabilities in the Thorpe's experiment

configuration [Thorpe 1969] are simulated to validate the model developed for the simulation of large interfaces within the multifield approach.

2. Computational model

In this section, the models used for the simulation of the large scale interfaces within the multifield approach are described.

2.1. Two-fluid model

The CFD calculations are based on an Eulerian approach with a finite volume discretization. The flow motion is followed using the two-fluid model of Ishii [1975] extended to n-phases. In this model, density, viscosity, volume fraction and local velocity are defined for each field in each cell. Here, we only consider laminar, isothermal and incompressible flows. Thus, density and viscosity are constant for a given field. To deal with flows with large interfaces, two conservation equations are solved for each continuous field k:

- The mass balance equation:

$$\partial_t(\alpha_k \rho_k) + \nabla.\left(\alpha_k \rho_k u_{i,k}\right) = \Gamma_k \qquad (1)$$

With α_k the volume fraction of field k, ρ_k its density, $u_{i,k}$ the i^{th} component of the velocity of field k and Γ_k the interfacial mass transfer of field k.

- The momentum equation:

$$\partial_t(\alpha_k \rho_k u_{i,k}) + \nabla.\left(\alpha_k \rho_k u_{i,k} u_{j,k}\right) = \nabla.(\alpha_k \mu_k S_k) - \alpha_k \nabla P + \alpha_k \rho_k g_i + I_{i,k} + F_{i,k} \quad (2)$$

With μ_k the viscosity of field k, S_k the viscous stress tensor, P the pressure, g the gravitational constant I the interfacial momentum transfer and F extra source terms due to the presence of large scale interfaces (surface tension) or coupling terms between the continuous fields (drag forces). The Continuum Surface Force (CSF) model proposed by Brackbill *et al.* [1992] and adapted to the two-fluid formulation [Bartosiewicz *et al.* 2008] has been used to model surface tension. A specific drag force law has been developed for the simulation of large interfaces within the two-fluid model. These two elements have been previously detailed and validated in Mimouni *et al.* [2014] and Fleau *et al.* [2015].

It is important to note that ρ_k and μ_k have the same value in the whole domain since they refer to the density and viscosity of each field. Thus, they are not affected by the existence of interfaces like in one-fluid formulations [Kataoka 1986].

Since we are dealing with incompressible flows, a common pressure is taken for all fields [Ishii 1975]. The following jump conditions are added to the two previous equations:

$$\sum_k \alpha_k = 1 \quad (3)$$

$$\sum_k \Gamma_k = 0 \quad (4)$$

$$\sum_k I_k = \frac{1}{\Omega} \int_{int} \sigma \, \kappa^{int} \, n^{int} dS \quad (5)$$

2.2. Interface sharpening equation

To limit the interface smearing, the interface sharpening equation proposed by Olsson and Kreiss [2005] is solved for each continuous field. For example, in a liquid/gas flow, the equation is solved for the continuous liquid field and the continuous gas field:

$$\partial_\tau \alpha_k + \nabla.(\alpha_k(1-\alpha_k)\boldsymbol{n}) = \epsilon \Delta \alpha_k \quad (6)$$

With **n** the interface normal vector:

$$\boldsymbol{n} = \frac{\nabla \alpha_k}{||\nabla \alpha_k||} \quad (7)$$

The interface sharpening equation is iteratively solved to ensure convergence of the prescribed interface thickness.

The values of the parameters $\Delta\tau$ and ϵ are calculated to obtain a final interface thickness always equal to 5 cells whatever the initial interface diffusion [Štrubelj 2009, Denèfle *et al.* 2015], as illustrated in Figure 1. In this article, the following values are taken:

$$\Delta\tau = \frac{\Delta x_{min}}{32} \quad \text{and} \quad \epsilon = \frac{\Delta x_{min}}{2} \quad (8)$$

With $\Delta x_{min} = \min\left(\Omega^{1/3}\right)$, for uniform meshes: $\Delta x = \Delta x_{min}$.

To illustrate the convergence of the equation and its ability to always obtain interfaces with 5 cells thickness, a bubble, with a diameter of 2 cm, is simulated in a still liquid with a square uniform Cartesian mesh of 5 cm side length. The interface is spread using the following diffusion

equation, which is iterated either 10, 20 or 50 times before being sharpened with the interface sharpening equation (6):

$$\partial_{\tau_1}\alpha_k = D_{diff}\nabla.(\nabla\alpha_k) \quad (9)$$

with $\Delta\tau_1 = 10^{-5}s$ and $D_{diff} = 0.1\, m^2.s^{-1}$. Thus, we observe in Figure 2 that whatever the mesh refinement and the initial interface diffusion, the final interface has always a thickness of 5 cells.

Only the iteration number of the interface sharpening equation varies according to the initial diffusion state. The mesh refinement does not increase the iteration number required to reach the final interface thickness.

Since the interface sharpening method is not restricted to uniform Cartesian grids, the same simulation has been performed with an unstructured grid obtained by Delaunay triangulation. The mesh contains 39734 cells. The air bubble is initially diffused with a linear variation of the volume fraction between two circles of radii 1.1 cm and 0.9 cm. The interface sharpening is solved to sharpen the interface until the recompression threshold is reached. At the end of the recompression step, we compare the positions of the isolines of the air volume fractions at 0.1, 0.5 and 0.9 obtained with the unstructured grid and two structured ones containing respectively 181 x 181 cells and 256 x 256 cells. The coarser structured mesh have a bit less cells than the unstructured grid and the refined structured grid approximately twice the cell number of the unstructured grid. Figure 3 shows that the bubbles obtained with the three grids are superimposed. This result confirms that the sharpening step is not restricted to Cartesian uniform grids and does not lose its efficiency on unstructured meshes.

3. Numerical method

The simulations are performed on fixed grids with collocated variables. The data structure is totally face-based, which allows the use of arbitrary-shaped cells including nonconforming meshes. Finite volume schemes are used to approximate space derivatives.

The well-known Semi-Implicit Method for Pressure-Linked Equations (SIMPLE) solver is implemented in the CFD tool [Patankar and Spalding 1972]. A schematic view of this algorithm is proposed in Figure 4 for adiabatic test cases dedicated to incompressible flows, which are in the scope of this article.

When the simulation starts, the boundary conditions are set. Then, an intermediate value of the velocity field is evaluated by solving the momentum equation (2) using the volume fractions and the pressure field at time step n. This intermediate velocity allows updating the volume fractions and the pressure field. To be consistent, these quantities are iteratively calculated within the so-called α-P loop (Figure 4) [Méchitoua *et al.* 2003 and Guelfi *et al.* 2007]. The final velocity field is then obtained by neglecting the convective and diffusive terms in the momentum equation (2) and considering the pressure increment.

More details about the numerical scheme can be found in Méchitoua *et al.* [2003] and Guelfi *et al.* [2007].

4. Implementation of the interface sharpening equation

4.1. Conservative implementation

A conservative implementation of the interface sharpening step is crucial to ensure mass conservation in the simulations. Thus, the numerical scheme has to be adapted (red box in

Figure 5 left). To understand how and where these changes occur, we will describe step by step the effect of the mass balance and the interface sharpening equations. At the end of the α-P loop, volume fractions have been updated by solving the following discretized mass balance equation (without mass transfers):

$$\rho_k \frac{\alpha_k^* - \alpha_k^n}{\Delta t} \Omega^I + \nabla.(\alpha_k^n \rho_k u_{i,k^*}) \Omega^I = 0 \quad (10)$$

with α_k^* the volume fraction of field k at the end of the α-P loop, α_k^n the volume fraction at time step n before the α-P loop, Δt the time step and Ω^I the cell volume. Let us introduce the following notation for the mass flux term $\nabla.\left(\alpha_k^n \rho_k u_{i,k^*}\right)\Omega^I = \sum_{IJ} \alpha_{IJ} \Phi_{IJ}$, such that the discretized mass balance equation can be written simply as a sum between an unsteady term and a mass flux term:

$$\rho_k \frac{\alpha_k^* - \alpha_k^n}{\Delta t} \Omega^I + \sum_{IJ} \alpha_{IJ} \Phi_{IJ} = 0 \quad (11)$$

Where $._{IJ}$ refers to the value at the cell faces between cell I and cell J.

After the α-P loop, the interface sharpening equation is solved using the intermediate volume fraction α_k^*. The discretized interface sharpening equation can also be expressed as a sum of an unsteady term and a mass flux term:

$$\frac{\alpha_k^{n+1} - \alpha_k^*}{\Delta \tau} \Omega^I + \sum_{IJ} \psi_{IJ} = 0 \quad (12)$$

With α_k^{n+1} the volume fraction of field k after the resolution of the interface sharpening equation, $\Delta \tau$ the characteristic time scale for the resolution of the interface sharpening equation

defined in Equation (7) and $\sum_{IJ}\psi_{IJ} = (\nabla.(\alpha_k^*(1-\alpha_k^*)\boldsymbol{n}) - \epsilon\Delta\alpha_k^*)\Omega^I$ the compressive and diffusive fluxes defined in the interface sharpening equation (6).

To ensure mass conservation, the total mass fluxes evaluated during a time step must correspond to the volume fraction distribution at the end of the time step, thus after the resolution of the interface sharpening equation. The mass fluxes calculated in this equation have to be added in the total mass fluxes such that:

$$\rho_k \frac{\alpha_k^{n+1} - \alpha_k^n}{\Delta t}\Omega^I + \sum_{IJ}\alpha_{IJ}^{'}\varphi_{IJ} = 0 \qquad (13)$$

With $\sum_{IJ}\alpha_{IJ}^{'}\varphi_{IJ}$ the total mass fluxes evaluated during a time step. By combining Equations (11) and (12), we obtain the expression of these mass fluxes:

$$\sum_{IJ}\alpha_{IJ}^{'}\varphi_{IJ} = \sum_{IJ}\alpha_{IJ}\Phi_{IJ} + \rho_{IJ}\frac{\Delta\tau}{\Delta t}\sum_{IJ}\psi_{IJ} \qquad (14)$$

Thus, these mass fluxes are determined at the end of the time step n. They are used in time step n+1 to predict the value of the velocity field (see Figure 5), as described in section 3 on the numerical method.

In a non conservative implementation, the total mass fluxes are not calculated at the end of time step n. Only the mass fluxes evaluated in the mass balance equation are used to predict the velocity field at time step n+1 (see Figure 5 right). The volume fractions α_k^{n+1} at the beginning of time step n+1 are not consistent with the value of the mass fluxes, which induces large discrepancies on mass conservation. As a consequence, this is a major drawback of most of CFD tools using an interface sharpening equation.

4.2. Recompression threshold

Two main phenomena are in competition when the interface sharpening equation is solved. The first one is mass conservation, which is ensured by the correction of the mass fluxes, described in the previous section. When the interface sharpening equation is implemented in a conservative way, the second important phenomenon is the addition of spurious velocities (besides the ones brought by the surface tension model) due to these mass fluxes, injected in the momentum balance equation, as illustrated in section 5.1.1. The objective of this part is then to find equilibrium between these opposite contributions and to reach a favourable effect on the simulations in terms of mass conservation and limitation of the spurious velocities. Thus, we propose to introduce a recompression threshold, which stops the resolution as soon as the final interface thickness is reached. As illustrated in Figure 2, up to a certain iteration number depending on the initial diffusion of the interface, the final thickness is reached. The extra iterations do not affect this thickness. This threshold allows limiting the quantity of mass fluxes added in the momentum balance equation for the prediction of the velocity field.

The recompression threshold is based on the ratio between the variation of the volume occupied by the interface and its initial volume: $\frac{\delta V_{int}}{V_{int}} < \beta \frac{\Delta x}{\Delta x_{min}}$. Thus, the criterion is evaluated at the interface, where $\alpha_l \alpha_g > 0.02$ and has the following expression:

$$\sum_{I}^{ncel} \delta\alpha_k^I (1 - 2\,\alpha_k^I)\Omega^I < \beta \frac{\Delta x}{\Delta x_{min}} \sum_{I}^{ncel} \alpha_l^I\, \alpha_g^I \Omega^I \qquad (15)$$

With α_k the volume fraction to which the interface sharpening is being applied and $\delta\alpha_k^I$ the volume fraction variation after each iteration of the interface sharpening equation. Since the equation is solved for each continuous field k, the criterion is applied for each continuous field.

In this expression, the term on the right-hand side $\sum_{I}^{ncel} \alpha_I^I \alpha_g^I \Omega^I$ denotes the volume occupied by the interface before the resolution of the interface sharpening equation. The term on the left-hand side $\sum_{I}^{ncel} \delta\alpha_k^I (1-\alpha_k^I)\Omega^I$ evaluates its variation after each iteration of the equation. The convergence is then obtained when the variation of the interface volume tends to zero, which corresponds to a coefficient β equal to zero computer error. Nevertheless, the conservative implementation of the interface sharpening equation induces a modification of the velocity field (see section 3 on the numerical method). Thus, if the equation is iterated many times, non zero mass fluxes are constantly added and result in the definition of spurious velocities. Therefore, the threshold β has to be optimized to allow an efficient interface sharpening with limited spurious velocities. This work will be undertaken in section 5 with different test cases.

Finally, we can notice that the term $\frac{\Delta x}{\Delta x_{min}}$ in the criterion of Equation (15) is equal to 1 for structured grids. For unstructured meshes, this additional term allows the increase of the recompression threshold in larger cells so that the recompression is stopped earlier. Indeed, in these cells, the interfaces will be considered badly resolved and will require a limited recompression effort.

4.3. Interface smearing criterion

The identification of the state of interface diffusion plays also an important role with the conservative formulation of the interface sharpening equation. Indeed, as previously developed with the recompression threshold, the resolution of the equation has to be limited to avoid adding mass fluxes, which will induce spurious velocities. Therefore, another criterion has been implemented to apply the interface sharpening equation only when a large interface is spread.

An interface is considered diffused if its thickness is higher than the thickness obtained after solving the interface sharpening equation, which is fixed at 5 cells. Therefore, the criterion is based on the value of the volume fraction gradient over the interface. Two conditions are then required to activate the compression equation resolution. The first one is to locate a large interface spread over few cells, which means to have cells in which $\alpha_l \alpha_g > 0.02$. In the picture (a) of Figure 6, this condition is not satisfied since $\alpha_l \alpha_g = 0$ everywhere in the domain. Therefore, the interface sharpening equation will not be solved for this type of interfaces.

If the first criterion is satisfied, then, in the cells containing the interface, the volume fraction gradient $\nabla \alpha_k^I . \boldsymbol{n}$, which is equal to $||\nabla \alpha_k^I||$, is evaluated and compared to $\frac{1}{5\Delta x}$. Indeed, as we can see in Figure 6 (b), $\frac{1}{5\Delta x}$ corresponds to the volume fraction gradient over an interface with a thickness of 5 cells. Therefore, if an interface is diffused, then its thickness will be higher than 5 cells (Figure 6 (c)). The volume fraction gradient will be smaller than $\frac{1}{5\Delta x}$.

5. Simulation results

In this section, we will illustrate the different steps presented in the previous section to implement the interface sharpening equation in the CFD tool. The first study will be devoted to the effect of a conservative implementation versus a non conservative one. For this purpose, a stationary bubble [Popinet 2009] and an oscillating air bubble [Caltagirone *et al.* 2011] will be simulated. Then, the recompression threshold will be examined with two other test cases: Bhaga's rising bubbles [Bhaga and Weber 1981] and the Kelvin-Helmholtz instabilities [Thorpe 1969]. Different values of the threshold β will be tested with different mesh refinements and time steps. The stationary bubble will allow evaluating the spurious velocities induced by the method. With the oscillating bubble, the oscillation frequency and the iteration number of the

interface sharpening equation will be compared. Then, the Bhaga's bubbles will be simulated to optimize the threshold value. Finally, a simulation of the Kelvin-Helmholtz instabilities, in the Thorpe's experiment configuration [Thorpe 1969], will be performed to study the effect of the criterion on the interface smearing. A validation of the threshold value is also detailed with this test case.

5.1. Simulation of a stationary bubble

The simulation of a stationary air bubble in liquid water has been performed to quantify the spurious velocities induced by the resolution of the interface sharpening equation. In this test case, the two continuous fields forming the interface are a liquid and a gas. The interface is initialized at equilibrium. All the fluids are at rest. Thus, the fluid velocities are supposed to be equal to zero. The bubble motion and the interface deformation are only due to spurious velocities. This test case is then particularly rough since, in most industrial configurations, the spurious velocities do not have a predominant effect on the observed phenomena. Indeed, the velocity intensities are usually higher thanks to the fluid motion.

The properties of the two fluids are given in Table 1. Surface tension coefficient is equal to 0.08 $N.m^{-1}$. The mesh is a square with 5 cm side length. The bubble is initialized with a round shape with a diameter of 2 cm.

5.1.1. Effect of a non conservative implementation

With the optimized threshold β, we can compare the benefit in terms of mass conservation of the conservative implementation compared to the addition of spurious velocities. For this comparison, the stationary bubble test case is simulated with a coarse mesh 64 x 64 cells. The

time step is equal to 0.1 ms. The mass balance error obtained by time step in the whole domain and the maximum value of the air velocity (see Equation (17)) after 1 s, representing the spurious velocity, are presented in Table 2 for the conservative and non conservative implementation of the interface sharpening equation. The spurious velocity intensity is increased by 13% when the interface sharpening equation is implemented in a conservative way. Therefore, the gain in mass error is larger than the increase of spurious velocity intensity induced by a conservative implementation.

5.1.2. Optimization of the threshold value $\boldsymbol{\beta}$

Then, the spurious velocities are evaluated for four different threshold values β: 1.10^{-4}, 5.10^{-4}, 1.10^{-3} and 1.10^{-2} and three different mesh refinements: 64 x 64 cells, 128 x 128 cells and 256 x 256 cells. The time step is equal to 0.1 ms, corresponding to a maximum CFL number of 0.9 for the more refined mesh. All the parameters studied in this test case (velocities and pressure) are evaluated at 1 s. Indeed, as shown in Figure 9, at 0.3 s, the bubble has already reached its equilibrium.

The capillary number is defined for the evaluation of the spurious velocities:

$$Ca = \frac{\mu_l U}{\sigma} \tag{16}$$

For the analysis of the spurious velocities, two definitions of U are considered. The first ones refers to a single-fluid approach definition of the spurious velocities. The velocity is considered in the air phase. It is evaluated where the phase is present, that is to say for $\alpha_g > 1.10^{-3}$. The average velocity and the maximum value are defined as followed:

$$|U| = \frac{\sum_{\alpha_g > 1.10^{-3}} \alpha_g \rho_g u_g}{\sum_{\alpha_g > 1.10^{-3}} \alpha_g \rho_g} \quad \text{and} \quad U_{max} = \max_{\alpha_g > 1.10^{-3}} (u_g) \qquad (17)$$

The second definition of U is based on the velocity of the air phase evaluated only within the interface thickness. This analysis is more suitable to the two-fluid model since the spurious velocities are only considered where the interfacial source terms, such as the drag force model, are applied. The following expressions are used to calculate the average and maximum value of U:

$$|U| = \frac{\sum_{\alpha_l \alpha_g > 0.1} \alpha_g \rho_g u_g}{\sum_{\alpha_l \alpha_g > 0.1} \alpha_g \rho_g} \quad \text{and} \quad U_{max} = \max_{\alpha_l \alpha_g > 0.1} (u_g) \qquad (18)$$

In Figure 7 (solid lines), the results are given by considering u = u_g (Equation (17)) for the definition of the spurious velocities, as done with single-fluid models in [Popinet 2009]. The X axis of the two graphs corresponds to the dimensionless quantity obtained by dividing the bubble diameter by the cell length. First, we see that, for coarse grid, the decrease of the threshold value does not ensure an accurate prediction of the velocity field. Thus, only an optimization of this parameter can improve the quality of the results by limiting the spurious velocities. Indeed, on the one hand, if the iteration number is low, the interface will require more compression at each time step and so induced more spurious velocities related to the sharpening step. This first situation concerns the threshold values $\beta = 1.10^{-2}$ for all the meshes (see Table 6) and explains the absence of convergence. On the other hand, if the number of iterations is high, non-zero mass fluxes continue to be added whereas the interface is enough sharpened. Once again, spurious velocities are created. This last situation explains the higher capillary number observed for the coarser mesh with $\beta = 1.10^{-4}$ (see Table 6).

In Figure 7 (dashed lines), the second point of view to evaluate the spurious velocities is proposed. We see that the same behaviour is observed when the mesh is refined or the threshold value is changed. The average and maximum values have the same order of magnitude at the interface and in the whole domain.

Finally, in Figure 8, a comparison of our results (solid lines in Figure 7 left) with other interface tracking methods is proposed. Thus, except with the VOF-PLIC method [Li 1995], the spurious velocities decrease with the mesh refinement. Moreover, for a given mesh refinement, the intensity of these velocities remains higher with the second gradient theory proposed by Jamet *et al.* [2000] than with the front-tracking method of Popinet and Zaleski [1999] and our method.

In Figure 9, we study the evolution of the spurious velocities over time [Jamet *et al.* 2002]. The simulations are performed with the intermediate mesh (128 x 128 cells). With $\beta = 1.10^{-3}$, $\beta = 5.10^{-4}$ and $\beta = 1.10^{-4}$, the capillary number oscillates slightly until 0.25 s before stabilizing.

The same observation can be done with $\beta = 1.10^{-2}$ but the variation range is higher. Indeed, since the interface sharpening equation is solved only once at each time step (see Table 6), the compression mass fluxes are larger and so induced more spurious velocities. Therefore, for $\beta \leq 1.10^{-3}$, the same behavior is observed since the compression is enough efficient at each time step.

Finally, for all the simulations, we study the error made in the prediction of the Laplace equation, given by:

$$P_{in} - P_{out} = \frac{\sigma}{R_n} \tag{19}$$

Where P_{in} is the pressure in the bubble and P_{out} out of the bubble, σ corresponds to the surface tension coefficient and R_n to the predicted final bubble radius.

To calculate P_{in} and P_{out}, the following expressions are used:

$$P_{in} = \frac{\sum_I^{ncel} \alpha_g^I P \Omega^I}{\sum_I^{ncel} \alpha_g^I \Omega^I} \quad \text{and} \quad P_{out} = \frac{\sum_I^{ncel} \alpha_l^I P \Omega^I}{\sum_I^{ncel} \alpha_l^I \Omega^I} \tag{20}$$

R_n, the final bubble radius, has the following expression:

$$R_n = \sqrt{\frac{S_n}{\pi}} \tag{21}$$

With S_n the estimated bubble area:

$$S_n = \sum_I^{ncel} \alpha_g^I \Delta x^2 \tag{22}$$

The results are displayed in Figure 10. Convergence is obtained whatever the threshold value. Contrary to the velocity field, the results are very close for the four threshold values and do not allow finding the best choice. To evaluate the order of convergence ξ of the pressure, we apply the following expression [Roache 1998], based on Richardson's extrapolation:

$$\xi = \frac{\ln\left(\frac{\Delta P_{m_3} - \Delta P_{m_2}}{\Delta P_{m_2} - \Delta P_{m_1}}\right)}{\ln\left(\frac{1}{2}\right)} \tag{23}$$

with m_1, m_2 and $m_3$three mesh refinements, such as:

$$\Delta x_{m_3} = \frac{\Delta x_{m_2}}{2} = \frac{\Delta x_{m_1}}{4} \quad (24)$$

Therefore, with $\beta = 1.10^{-2}$, the order of convergence is equal to 1.6, with $\beta = 1.10^{-3}$ to 1.4, with $\beta = 5.10^{-4}$and $\beta = 1.10^{-4}$ to 0.9.

To conclude, these two illustrations show that the threshold value must be carefully chosen to allow an efficient interface sharpening without adding too many spurious velocities. The mesh refinement study highlights that an appropriate value can be chosen between 1.10^{-3} and 5.10^{-4}.

5.2. Simulation of an oscillating bubble

5.2.1. Effect of a non conservative implementation

To highlight the effect of the conservative implementation on mass conservation and physical results, an oscillating air bubble in a still liquid has been simulated without gravity (see Table 3 for the fluid properties) [Caltagirone *et al.* 2011]. Once again, we simulate an interface between a continuous liquid field and a continuous gas field. Surface tension coefficient is equal to 1.5 $N.m^{-1}$. The mesh is a square with 5 cm side length. The bubble is initialized with an ellipsoidal shape with a semi-minor axis equal to 0.95 cm and a semi-major axis of 1.05 cm.

The interfacial position of the bubble is given in polar coordinates by Lamb [1932]:

$$r(\theta, t) = R_0 \left(1 + \tilde{\epsilon} \cos(2\theta) \cos(\omega_d t) \exp\left(-\frac{t}{\tau_d}\right) \right) \quad (25)$$

With R_0 the final bubble radius equal to 1 cm, $\tilde{\epsilon}$ the initial perturbation of the bubble equal here to 0.05, θ the angular coordinate, ω_d the oscillation frequency and τ_d the characteristic time of decay due to viscous damping:

$$\omega_d{}^2 = \frac{6\sigma}{R_0{}^3(\rho_l + \rho_g)} \quad \text{and} \quad \tau_d = \frac{R_0{}^2(\rho_l + \rho_g)}{4(\mu_l + 3\mu_g)} \tag{26}$$

With the fluid properties given in Table 3, the expected bubble frequency is equal to 5.71 s^{-1} and the characteristic time of decay to 4.37 s.

The oscillating bubble is simulated with two different meshes: 128 x 128 cells and 256 x 256 cells with a conservative implementation of the interface sharpening equation and a non conservative one. For the two simulations, the optimized value of the recompression threshold β determined in section 5.2.2 is taken. The time steps are constant and given in Table 4. Smaller values are used for the non conservative approach to ensure that the Courant–Friedrichs–Lewy (CFL) number is kept under 0.9. The evolution of the major axis of the bubble is displayed in Figure 11. We observe irregularities on the curves corresponding to the non conservative implementation. They are due to spurious oscillations of the bubble in diagonal directions. Moreover, the decay of the oscillation amplitude is quicker with the non conservative implementation. More quantitatively, in Table 5, we compare the oscillation frequency and the characteristic time of decay for the two grids, the two implementation of the interface sharpening equation and with the results of Caltagirone *et al.* [2011]. These two parameters are underestimated by the non conservative approach.

This comparison is made on a relatively simple test case without turbulence effects and phase change. Nevertheless, a non conservative implementation can have heavier consequences on more complicated cases. As an example, when dealing with interfaces with phase change, the

non conservative approach induces numerical instabilities while interface velocities are larger than the spurious velocities. Therefore, the conservative implementation is also of great importance for two-phase flows problems in complex industrial configurations since we are often dealing with boiling interfaces.

Finally, concerning mass conservation, the mass balance error by time step in the whole domain is equal to 10^{-11} % with the non conservative approach and is reduced at 10^{-17} % with the conservative approach.

To conclude, this study confirms that the non conservative implementation of the interface sharpening equation does not ensure mass conservation to almost computer error. Moreover, not considering the mass fluxes appearing in the recompression equation affects badly the simulations by decreasing the accuracy of the results.

5.2.2. Optimization of the threshold value β

In a second study, we propose to compare four different values of the recompression threshold β: 1.10^{-4}, 5.10^{-4}, 1.10^{-3} and 1.10^{-2}. Three different mesh refinements are used: 64 x 64 cells, 128 x 128 cells and 256 x 256 cells. The time step is kept constant and is respectively equal to 0.05 ms, 0.025 ms and 0.0125 ms.

In Table 6, the iteration number is displayed for each mesh and threshold value. We observe first that the larger β is, the less the interface sharpening equation is iterated. This confirms that the criterion does its work to limit the equation resolution. Moreover, the iteration number decreases with the mesh refinement for a given threshold value. Indeed, the mesh refinement reduces the numerical diffusion and so the sharpening effort. Then, in Table 7, we compare the oscillation

frequency of the bubble. For $\beta = 1.10^{-4}$, the oscillation frequency is only given for the more refined mesh. Indeed, with the two other meshes, the bubble moves in the domain instead of oscillating regularly as expected. This phenomenon is caused by the high number of iterations of the interface sharpening equation, which induces the accumulation of spurious recompression mass fluxes since the interface required less iterations to be enough sharpened. These mass fluxes are injected in the momentum balance equation used to predict the velocity and induce spurious velocities. The mesh refinement reduces this iteration number and so the spurious velocities, allowing the bubble oscillation. For $\beta = 1.10^{-2}$, we observe that the prediction of the oscillation frequency becomes more accurate with the mesh refinement. With $\beta = 1.10^{-3}$ and $\beta = 5.10^{-4}$, we also see this convergence. Nevertheless, for the intermediate and the refined mesh, the same frequency is obtained due to the accuracy of the method. For the coarser mesh, the oscillation frequency given here must be nuanced since we observe some spurious oscillations and displacements of the bubbles. The results obtained with these three values of β are in good agreement with the theory. However, with $\beta = 1.10^{-2}$, the lack of interface recompression results in a numerical fragmentation of the bubble interface, as shown in Figure 12. To conclude, values $\beta = 1.10^{-3}$ and $\beta = 5.10^{-4}$ are two potential candidates to define an optimized recompression threshold.

In a second study, we observe the effect of the time step choice for one mesh refinement (128 x 128 cells) and one threshold value $\beta = 1.10^{-3}$. Three time steps are simulated: 0.025 ms, 0.0125 ms and 0.01 ms. The results are given in Table 8. We see a good convergence of the oscillation frequency when the time step decreases. Moreover, with a time step equal to 0.0125 ms, the interface sharpening equation is iterated only once like in the previous study with the same mesh but $\beta = 1.10^{-2}$ and a time step of 0.025 ms. Nevertheless, in this particular case, the prediction of the oscillation frequency is more accurate. Indeed, since the time step is reduced, the numerical diffusion at each time step is smaller. Thus, the interface needs less

recompression iterations to be sharpened. Therefore, the interface is more efficiently sharpened at each time step, which conducts to a more accurate prediction of the bubble motion. On the contrary, with the larger time step, the interface will be slightly thicker after one iteration of the interface sharpening equation. After a given duration of the simulation, this effect will be amplified, resulting in a less accurate interface location compared to a smaller time step. This effect can be seen in Figure 2. For a given iteration number (at the beginning of the recompression process), the final interface thickness is proportional to its initial width. Thus, the interfaces, which are initially more diffused, that is to say in our context which have been obtained with a larger time step, are less sharpened after a given iteration number (equal to one here) of the recompression equation. We can note that in Figure 2, this phenomenon is amplified since we are studying much thicker interfaces than in this test case. No differences are observed with 0.0125 ms and 0.01 ms due to the precision of the method used to determine the oscillation frequency.

To conclude, this study highlights that an optimal value for β has to be chosen. Indeed, if β is too low, non negligible spurious velocities are introduced which affect the bubble oscillations. On the contrary, if β is too large the interface is not well sharpened. $\beta = 1.10^{-3}$ and $\beta = 5.10^{-4}$ are two potential candidates to obtain an optimized recompression threshold. Finally, we showed that for more refined grid or smaller time steps, interfaces required less sharpening since they are less diffused at each time step.

5.3. Simulation of the Bhaga's rising bubbles test case

To optimize the threshold value, an extra simulation is proposed with Bhaga's rising bubbles test case [Bhaga and Weber 1981]. This test case contains also an interface between a liquid phase and a gas phase, which are the two continuous fields.

In this test case, an air bubble is rising up in viscous water. For this simulation, the properties of the two fluids are: $\rho_l = 1350\ \mathrm{kg.m^{-3}}$, $\rho_g = 1.35\ \mathrm{kg.m^{-3}}$ and $\mu_g = 1.8.10^{-5}$ Pa.s. Surface tension is equal to 0.0785 $\mathrm{N.m^{-1}}$. Two cases have been tested with two different Reynolds numbers and liquid viscosities (see Table 9).

An hydrostatic pressure is imposed in the column:

$$\mathrm{P} = P_o + \rho_l g(z_{max} - z) \qquad (27)$$

With P_o the atmospheric pressure.

In the Bhaga's experiment, the bubble had an initial volume of 9.3 $\mathrm{cm^3}$. Therefore, in the assumption of spherical bubbles, the bubble radius is initialized at 1.3 cm in our simulations. Moreover, the bubble is initially located at 3.9 cm from the top of the mesh, which corresponds to three radii.

The dimensions of the computational domain are chosen large enough (four times the bubble diameter) to avoid wall effects on the bubble and high enough (12 times the bubble diameter) to reach the limit velocity [Hua and Lou 2007]. Therefore, to limit CPU consumption, a 2D axisymmetric mesh, whose definition sketch is given in Figure 13, is used. The mesh contains 179 x 540 cells. Thus, the initial bubble radius is around equal to 23 cells. The mesh length depends on the case: L = 10.38 cm for case b and L = 10.33 cm for case d. Indeed, the symmetric axis is difficult to compute since the mesh dimension in the y direction is very small in this zone. Thus, the deformation of the bubble is not well predicted in this region especially in case d since the liquid viscosity is smaller, which induces more bubble

deformations. A mesh truncation is adopted, equal to 0.2 mm for case b and 0.7 mm for case d. The time step is kept constant, equal to 1.10^{-5} s for case b and 1.10^{-4} s for case d to have a maximum CFL number equal to 0.9. Because the mesh is less truncated for case b, the mesh dimensions are smaller close to the symmetry axis and the time step has to be smaller.

For the first study, case d is simulated with three different threshold values: 5.10^{-3}, 1.10^{-3} and 5.10^{-4}. Indeed, Denèfle *et al.* [2015] showed that this case was more challenging in terms of bubble shape prediction.

To analyze the results, the final shape of the bubble (at 0.6 s) and its average velocity are compared to Bhaga's experimental data. To evaluate the average bubble velocity u, the following expression is used:

$$\mathrm{u} = \frac{\sum_I^{ncel} \alpha_g^I \, u_g^I \Omega^I}{\sum_I^{ncel} \alpha_g^I \, \Omega^I} \tag{28}$$

The simulated bubbles are superimposed to the experimental results [Bhaga and Weber 1981] in Figure 14. The first threshold value 5.10^{-3} (Figure 14 (a)) induces a non physical elongation of each bubble side due to the lack of compression at each time step. The second threshold value 1.10^{-3} corrects this effect. Nevertheless, the bubble extremities remain not enough sharpened and detached twice (see Figure 14 (b)). Thus, at 0.6 s, the final bubble volume is smaller than expected. Moreover, these detachments slow down the bubble, which has a final velocity equal to 28.3 $cm.s^{-1}$ compared to the experimental value (deducted from the Reynolds number) of 29 $cm.s^{-1}$. Therefore, the threshold value is one more time decreased at 5.10^{-4} (Figure 14 (c)). We see that the prediction is in reasonable agreement with the experimental data. Moreover, the simulated final velocity is equal to 28.9 $cm.s^{-1}$, which corresponds to a relative error of 0.3 %.

Case b is also simulated with $\beta = 5.10^{-4}$. The bubble shape is shown in Figure 15. The simulation results agree well with the Bhaga's experimental data. Furthermore, the final velocity is found equal to 24.5 cm.s^{-1}, corresponding to a relative error of 19.5% (experimental final velocity 20.5 cm.s^{-1}).

In terms of recompression efficiency, we see in Figure 2 that whatever the mesh refinement and the initial interface diffusion, the final thickness is reached by fixing the recompression threshold at 5.10^{-4}. Thus, for the following simulations, the threshold value is fixed at 5.10^{-4}.

Finally, we can note that, with the conservative implementation of the interface sharpening equation, the mass balance error by time step in the whole domain is equal to 10^{-16} %.

5.4. Simulation of Thorpe's experiment

5.4.1. Effect of the interface smearing criterion

The Kelvin-Helmholtz instabilities in Thorpe's experimental configuration [Thorpe 1969] are a good example of an interface with limited diffusion. Indeed, in this test case, two immiscible fluids are contained in a rectangular box, which is tilted for a small angle, $\sin(\gamma) = 0.072$, as displayed in Figure 16. The velocities of each fluid vary in opposite directions.

These velocities conduct to the existence of a shear stress at the interface, which prevents it against diffusion. Moreover, this simulation illustrates another type of interfaces between two continuous liquid fields.

The theory of the Kelvin-Helmholtz instabilities is based on the inviscid fluid flow theory with:

$$\rho = \begin{cases} \rho_2 & \text{for } 0 < z < h \\ \rho_1 & for\ h < z < H \end{cases} \quad (29)$$

With $\mathrm{h} = \mathrm{h}_1 = \mathrm{h}_2 = \frac{\mathrm{H}}{2} = 1.5\ cm$.

The steady velocity distribution along the rectangular tube is:

$$u = \begin{cases} -\dfrac{\Delta u}{2} & for\ 0 < z < h \\ \dfrac{\Delta u}{2} & for\ h < z < H \end{cases} \quad (30)$$

This parallel flow is assumed to be a solution of Euler equations upon which is superposed a small perturbation proportional to $\exp(\mathrm{i}(\mathrm{kx} + \omega \mathrm{t}))$ with k a wavenumber and ω a pulsation. The linearization of the Euler equations gives the following dispersion relation:

$$\omega = k\frac{\Delta u(\rho_2 - \rho_1)}{2(\rho_1 + \rho_2)} \pm \sqrt{\frac{\sigma k^3 + gk(\rho_2 - \rho_1)}{(\rho_1 + \rho_2)}\mathrm{th}(kh) - \frac{k^2 \Delta u^2 \rho_1 \rho_2}{(\rho_1 + \rho_2)^2}} \quad (31)$$

The system becomes unstable when the relative velocity between the two fluids exceeds a critical velocity, given by the following equation [Thorpe 1969]:

$$\Delta u^2 > \frac{(\rho_1 + \rho_2)}{\rho_1 \rho_2}\left(\sigma k + \frac{g(\rho_2 - \rho_1)}{k}\right)\ \mathrm{th}(kh) \quad (32)$$

With σ = 0.04 $\mathrm{N.m^{-1}}$ the surface tension coefficient and k_c the critical wavenumber:

$$k_c = \sqrt{\frac{g(\rho_2 - \rho_1)}{\sigma}} \tag{33}$$

Moreover, the analytical velocity distribution in the whole domain at the beginning of the simulation, when the linear regime can be assumed, is:

$$\begin{cases} u_2 = -\dfrac{(\rho_2 - \rho_1)h_1 g \sin(\gamma)}{(\rho_1 h_2 + \rho_2 h_1)} t \quad for\ 0 < z < h \\ u_1 = \dfrac{(\rho_2 - \rho_1)h_2 g \sin(\gamma)}{(\rho_1 h_2 + \rho_2 h_1)} t \quad for\ h < z < H \end{cases} \tag{34}$$

The properties of the two fluids are: $\rho_1 = 780\ \text{kg.m}^{-3}$, $\mu_1 = 1.5.10^{-3}$ Pa.s, $\rho_2 = 1000\ \text{kg.m}^{-3}$ and $\mu_1 = 1.10^{-3}$ Pa.s. The dimensions of the computational domain are H = 3 cm and L = 1.83 m (see Figure 16). The mesh contains 80 x 4880 cells. The simulation is performed with a constant time step equal to 0.5 ms, which ensures that the CFL number stays under 0.9.

Two simulations are considered: one with a criterion on the interface smearing, which limits the recompression of diffused interfaces and another without this criterion. The evolution of the interface shape for the two cases is displayed in Figure 17. No differences are observed between the two pictures. The interface deformation is similar with and without the criterion.

The interface profile at 3 s is then extracted to determine the critical wavenumber (see Figure 18). Therefore, the critical wavenumber obtained without the criterion is equal to 202 m^{-1} and

to 219 m^{-1} with the criterion. These results are both in good agreement with the experimental, theoretical and simulated data (see Table 10).

The time of the instability onset t_{onset} is also compared. For this purpose, the standard deviation of the interface is evaluated every 0.2 s between 1 s and 3.4 s. The results are shown in Figure 19. In the two simulations, the time of the instability onset is equal to 2.1 s.

Then, Figure 20 presents the maximum value of the average interface velocity U over time defined as followed:

$$U = \frac{\alpha_1 \rho_1 u_1 + \alpha_2 \rho_2 u_2}{\alpha_1 \rho_1 + \alpha_2 \rho_2} \quad (35)$$

This velocity refers to a weighted average of the fluid velocities at the interface. The results are compared with Equation (34), which is valid at short times, where the linear approximation can be applied. Therefore, we see that the two simulations predict well the evolution of this velocity.

Finally, the wave speed u_{waves} is compared by calculating the crest-to-crest distance at different positions in the tank. Figure 21 gives an example of the waves used for this calculation. We find u_{waves} = 1.6 $cm.s^{-1}$ without the criterion and u_{waves} = 3.1 $cm.s^{-1}$ with the criterion. In comparison with the experimental, theoretical and simulated data displayed in Table 10, the simulation without the criterion does not well predict this parameter.

Thus, we see that the criterion controlling the activation of the interface sharpening equation does not change dramatically the simulations. However, it can affect some specific parameters such as the surface wave speed. Therefore, to simulate accurately such flows, the activation of the recompression equation is restricted to diffused interfaces.

5.4.2. Validation of the threshold value β

With the Bhaga's rising bubble test case, we showed that $\beta = 5.10^{-4}$ gave the best results in terms of final bubble velocity and bubble shape. However, the results obtained with $\beta = 1.10^{-3}$ were also quite close to the experimental data. Therefore, to validate the choice of $\beta = 5.10^{-4}$, we compare the two values with the Thorpe's experiment test case. This new comparison allows a validation on a different flow type since the Thorpe's experiment is an interfacial liquid/liquid test case. The critical wavenumber, the time of the instability onset and the wave velocity are extracted from the interface motion, as detailed previously. The results are displayed in Table 10. The time of the instability onset and the critical wavenumber are close for the two threshold values. Nevertheless, the simulation with $\beta = 1.10^{-3}$ predicts a smaller wave speed. The threshold value $\beta = 5.10^{-4}$ seems appropriate for the simulation of different flow types.

Finally, we can note the effect of the conservative implementation of the sharpening equation. Indeed, the mass balance error by time step in the whole domain decreases by 10^{-10} % with a non conservative implementation to 10^{-17} %.

6. Conclusion

The development of a multifield approach requires the ability to locate accurately large interfaces for multiscale multiphase flows. Nevertheless, the two-fluid model, implemented in the CFD tool NEPTUNE_CFD, induced in its initial version a smearing of these interfaces. Therefore, the implementation of an interface sharpening equation combined with an appropriate drag force model were necessary to ensure an accurate simulation. Thus, in this paper, different combinations and parameters of the interface sharpening equation have been

compared with four adiabatic laminar test cases. A summary of the simulations is displayed in Table 11. This study highlighted first the importance of a conservative implementation to ensure mass conservation. As an example, the simulations of the Thorpe's experiment with a non conservative formulation produced a mass balance error by time step in the whole domain equal to 10^{-10} %. This error was reduced to 10^{-17} % with a conservative implementation. Nevertheless, it has been shown that the conservative implementation had an impact on the evaluation of the velocity fields through the addition of compression mass fluxes. Therefore, the resolution of the interface sharpening equation had to be limited to avoid creating spurious velocities by adding extra mass fluxes while, at the same time, ensuring a sufficient interface sharpening. For this purpose, two criteria have been developed. The first one concerns the equation convergence and is based on the volume variation of the interface induced by the compression. An analysis of the spurious velocities with a stationary bubble test case followed by a validation with Bhaga's rising bubble (a large bubble simulation) and Thorpe's experiment (an interfacial liquid/liquid test case) allowed optimizing the value of the threshold β used to stop the resolution of the interface sharpening equation. This value was fixed at 5.10^{-4}. The second criterion evaluates the state of the interface smearing thanks to the volume fraction gradient and has been validated with the simulation of the Thorpe's experiment.

Thus, these recent developments are a first step in the simulations of multiphase flows. Further studies should be performed on the one hand to apply this numerical modeling to large interfaces with heat and mass transfer like sucking or Stefan problems [Welch and Wilson 2000 and Fleau 2017]. For these applications, an energy equation is solved in addition to the mass balance, momentum and interface sharpening equations. On the other hand, specific developments are under investigation concerning interface and turbulence interactions. This work aims at simulating complex flows with a full system perspective, for

example a steam generator, by dealing precisely with all the coupling terms between the different representations of the two-phase flow in a Large Eddy Simulation (LES) framework [Sagaut and Germano 2005, Denèfle *et al.* 2015 and Fleau 2017].

Acknowledgments

The results presented in this paper have been obtained with the CFD tool NEPTUNE_CFD, developed in the framework of the NEPTUNE project, financially supported by CEA (Commissariat l'Énergie Atomique et aux Energies Alternatives), EDF (Électricité de France), IRSN (Institut de Radioprotection et de Sûreté Nucléaire) and AREVA NP, in collaboration with MSME laboratory (Université Paris-Est, Champs sur Marne, France). We are grateful for access to the computational facilities of the french CINES (National computing center for higher education) and CCRT (National computing center of CEA) under project number x20172b6115.

References

Anderson, T. B. and Jackson, R. [1967], Fluid mechanical description of fluidized beds. Equations of motion, *Ind. Eng. Chem. Fundam.*, Vol. 6, Issue 4, pp. 527-539.

Bartosiewicz, Y., Laviéville, J. and Seynhaeve, J.M. [2008], A first assessment of the NEPTUNE_CFD code: Instabilities in a stratified flow comparison between the VOF method and a two-field approach, *Int. J. Heat and Fluid Flow*, Vol. 29, pp. 460-478.

Bhaga, D. and Weber, M.E. [1981], Bubbles in viscous liquids: shape, wakes and velocities, *J. of Fluid Mech*., Vol. 105, pp. 61-85.

Borniaa, G., Cervone, A., Manservisi, S., Scardovelli, R. and Zaleski, S. [2011], On the properties and limitations of the height function method in two-dimensional Cartesian geometry, *J. Comput. Phys.*, Vol. 230, Issue 4, pp. 851-862.

Brackbill, J. U., Kothe, D. B. and Zemach, C. [1992], A continuum method for modeling surface tension, *J. Comput. Phys.*, Vol. 100, pp. 335–354.

Caltagirone, J.P., Vincent, S. and Caruyer, C. [2011], A multiphase compressible model for the simulation of multiphase flows, *Comput. Fluids*., Vol. 50, pp. 24-34.

Capecelatro, J., Pepiot, P. and Desjardins, O. [2010], Eulerian-Lagrangian Simulations of Three-Dimensional Turbulent Riser Flows, Proceedings of the 63rd Annual Meeting of the APS Division of Fluid Dynamics, Long Beach, California.

Dabiri, S. and Tryggvason, G. [2015], Heat transfer in turbulent bubbly flow in vertical channels, *Chem. Eng. Sc.*, Vol. 122, pp. 106-113.

Denèfle, R., Mimouni, S., Caltagirone, J.P. and Vincent, S. [2015], Multifield hybrid approach for two-phase flow modeling – Part 1: Adiabatic flows, *Comput. Fluids*., Vol. 113, pp. 106-111.

Di Bari, S., Lakehal, D. and Robinson, A.J. [2013], A numerical study of quasi-static gas injected bubble growth: Some aspects of gravity, *Int. J. Heat Mass Transf.*, Vol. 64, pp. 468-482.

Drew, D. A. and Lahey, R. T. [1979], Application of general constitutive principles to the derivation of multidimensional two-phase flow equations, *Int. J. Multiphase Flow*, Vol. 5, Issue 4, pp. 243-264.

Fleau, S., Mimouni, S., Mérigoux, N. and Vincent, S. [2015], Validation of a multifield approach for the simulations of two-phase flows, *Comput. Therm. Sci.*, Vol. 7, Issue 5-6, pp. 441-457.

Fleau, S. [2017], Multifield approach and interface locating method for two-phase flows in nuclear power plant, *PhD Thesis*, University of Paris-Est Marne-la-Vallée, EDF R&D.

Guelfi, A., Bestion, D., Boucker, M., Boudier, P., Fillion, P., Grandotto, M., Hérard, J.M., Hervieu, E. and Péturaud, P. [2007], NEPTUNE - A new software platform for advanced nuclear thermal hydraulics, *Nucl. Sci. Eng.*, Vol. 156, pp. 281-324.

Hänsch, S., Lucas, D., Krepper, E. and Höhne, T. [2012], A multi-field two-fluid concept for transitions between different scales of interfacial structures, *Int. J. Multiphase Flow*, Vol. 47, pp. 171-182.

Hao, J., Chen, W., Zhang, D. and Wang, S. [2014], Scaling modeling analysis of flow instability in U-tubes of steam generator under natural circulation, *Ann. Nucl. Energy*, Vol. 64, pp. 169-175.

Herrmann, M. [2010], A parallel Eulerian interface tracking/Lagrangian point particle multi-scale coupling procedure, *J. Comput. Phys.*, Vol. 229, pp. 745–759.

Hua, J. and Lou, J. [2007], Numerical simulation of bubble rising in viscous liquid, *J. Comput. Phys.*, Vol. 222, pp. 769-795.

Ii, S., Sugiyama, K., Takeuchi, S., Takagi, S., Matsumoto, Y. and Xiao, F. [2011], An interface capturing method with a continuous function: The THINC method with multi-dimensional reconstruction, *J. Comput. Phys.*, Vol. 231, pp. 2328-2358.

Ishii, M. [1975], *Thermo-fluid dynamic, theory of two-phase flow*, Eyrolles.

Jamet, D., Lebaigue, O., Coutris, N. and Delhaye, J.M. [2000], Feasibility of using the second gradient theory for the simulation of liquid-vapor with phase change, *J. Comput. Phys.*, Vol. 169, pp. 624-651.

Jamet, D., Torres, D. and Brackbill, J. U. [2002], On the Theory and Computation of Surface Tension: The Elimination of Parasitic Currents through Energy Conservation in the Second-Gradient Method, *J. Comput. Phys.*, Vol. 182, Issue 1, pp. 262-276.

Kataoka, I. [1986], Local instant formulation of two-phase flow. *Int. J. Multiphase Flow*, Vol. 12, pp. 745–758.

Lamb, H. [1932], *Hydrodynamics*, 6th Edition of Cambridge University Press.

Lebas, R., Ménard, T., Beau, P.A., Berlemont, A. and Demoulin, F.X. [2009], Numerical simulation of primary break-up and atomization: DNS and modelling study, *Int. J. Multiphase Flow*, Vol. 35, Issue 3, pp. 247-260.

Li, J. [1995], Calcul d'interface affine par morceaux (piecewise linear interface calculation), *C. R. Acad. Sci. Paris*, Série IIb, Vol. 320, pp. 391-396.

Ling, Y., Zaleski, S. and Scardovelli, R. [2015], Multiscale Simulation of Atomization with Small Droplets Represented by a Lagrangian Point-Particle Model, *Int. J. Multiphase Flow*, Vol. 76, pp. 122-143.

Ma, Y., Li, X. and Wu, X. [2014], Thermal–hydraulic characteristics and flow instability analysis of an HTGR helical tube steam generator, *Ann. Nucl. Energy*, Vol. 73, pp. 484-495.

Méchitoua, N., Boucker, M., Laviéville, J., Pigny, S. and Serre, G. [2003], An unstructured finite volume solver for two phase water/vapour flows based on an elliptic oriented fractional

step method, Proceedings of the 10th Int. Topl. Mtg. Nuclear Reactor Thermal Hydraulics (NURETH 10), Seoul, Republic of Korea.

Mimouni, S., Laviéville, J., Seiler, N. and Ruyer, P. [2011], Combined evaluation of second order turbulence model and polydispersion model for two-phase boiling flow and application to fuel assembly analysis, *Nucl. Eng. Des.*, Vol. 241, Issue 11, pp. 4523-4536.

Mimouni, S., Denèfle, R., Fleau, S. and Vincent, S. [2014], Multifield approach and interface locating method for two-phase flows in nuclear power plant, in Advances in Hydroinformatics, SIMHYDRO2014.

Nonomura, T., Kitamura, K. and Fujiia, K. [2014], A simple interface sharpening technique with a hyperbolic tangent function applied to compressible two-fluid modelling, *J. Comput. Phys.*, Vol. 258, pp. 95-117.

Olsson, E. and Kreiss, G. [2005], A conservative level set method for two phase flow, *J. Comput. Phys.*, Vol. 210, pp. 225-246.

Patankar, S. and Spalding, D. [1972], A calculation procedure for heat, mass and momentum transfer in three-dimensional parabolic flows, *Int. J. Heat Mass Transf.*, Vol. 15, Issue 10, pp. 1787-1806.

Popinet, S. and Zaleski, S. [1999], A front-tracking algorithm for accurate representation of surface tension, *Int. J. Numer. Meth. Fluids*, Vol. 30, pp. 775-793.

Popinet, S. [2009], An accurate adaptive solver for surface-tension-driven interfacial flows, *J. Comput. Phys.*, Vol. 228, Issue 16, pp. 5838-5866.

Roache, P.J. [1998], *Verification and Validation in Computational Science and Engineering*, Hermosa Publishers.

Sagaut, P., and Germano, M. [2005], On the filtering paradigm for LES of flows with discontinuities, *J. Turb.*, Vol. 6, Issue 23.

Saurel, R. and Abgrall, R. [1999], A Multiphase Godunov Method for Compressible Multifluid and Multiphase Flows, *J. Comput. Phys.*, Vol. 50, Issue 2, pp. 425-467.

So, K.K., Hu, X.Y. and Adams, N.A. [2011], Anti-diffusion method for interface steepening two-phase incompressible flow, *J. Comput. Phys.*, Vol. 230, pp. 5155-5177.

Štrubelj, L. [2009], Numerical simulations of stratified two-phase flows with two-fluid model and interface sharpening, *M.Sc. Thesis*, University of Ljublana.

Thorpe, S. [1969], Experiments on the instability of stratified shear flows: immiscible fluids, *J. Fluid Mech.*, Vol. 39, pp 25-48.

Tomar, G., Fuster, D., Zaleski, S. and Popinet, S. [2010], Multiscale simulations of primary atomization, *Comput. Fluids*., Vol. 39, Issue 10, pp. 1864-1874.

Vallet, A. and Borghi, R. [1999], Modélisation Eulérienne de L'atomisation d'un Jet Liquide, *C. R. Acad. Sci. Paris*, Série IIb, Vol. 327, Issue 10, pp. 1015-1020.

Wang, Z.L., Tian, W.X., Wu, Y.W., Qiu, S.Z. and Su, G.H. [2012], Numerical study on annular tube once-through steam generator using compressible flow model, *Ann. Nucl. Energy*, Vol. 39, Issue 1, pp. 49-55.

Watanabe, T., Anoda, Y. and Takano, M. [2014], System–CFD coupled simulations of flow instability in steam generator U tubes, *Ann. Nucl. Energy*, Vol. 70, pp. 141-146.

Welch, S.W.J. and Wilson, J. [2000], A Volume of fluid based method for fluid flows with phase change, *J. Comput. Phys.*, Vol. 160, pp. 662-682.

Xiao, F., Honma, Y. and Kono, T. [2005], A simple algebraic interface capturing scheme using hyperbolic tangent function, *Int. J. Numer. Meth. Fluids*, Vol. 48, Issue 9, pp. 1023-1040.

Xiao, F., Ii, S. and Chen, C. [2011], Revisit to the THINC scheme: A simple algebraic VOF algorithm, *J. Comput. Phys.*, Vol. 230, pp. 7086–7092.

Zuzio, D., Estivalezes, J.L., Villedieu, P. and Blanchard, G. [2013], Numerical simulation of primary and secondary atomization, *C. R. Mécanique*, Vol. 241, pp. 15-25.

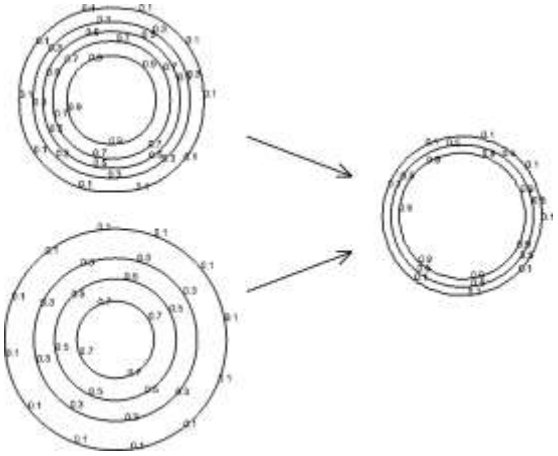


Figure 1. Sensitivity of the interface sharpening method, left: two interfaces with two different initial thicknesses, right: final thickness of the two interfaces after resolution of the interface sharpening equation.

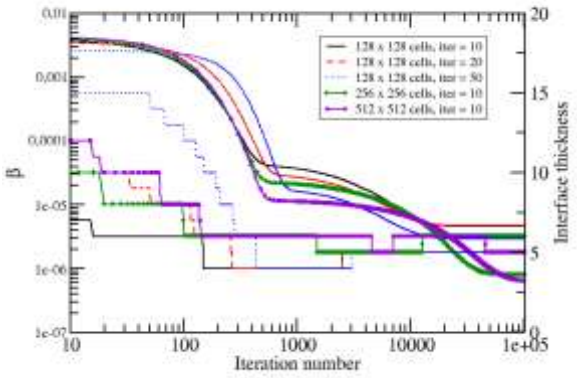


Figure 2. Effect of the interface sharpening equation on interfaces with different initial diffusions and with different mesh refinements, the right axis refers to the quantity β, which represents the ratio between the volume variation of the interface after each iteration of the interface sharpening equation and the initial interface volume, the interface thickness in the left axis is given in cell numbers, iter refers to the iterations of the diffusion equation, the higher iter, the more diffused the interface.

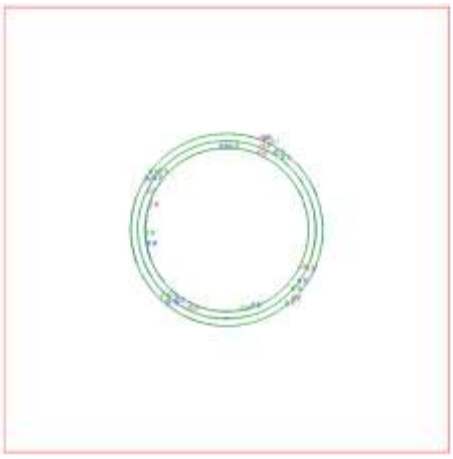


Figure 3. Isolines of the air volume fractions at 0.1, 0.5 and 0.9 obtained on an unstructured grid with 39734 cells (red) and two structured grid with respectively 181 x 181 cells (blue) and 256 x 256 cells (green).

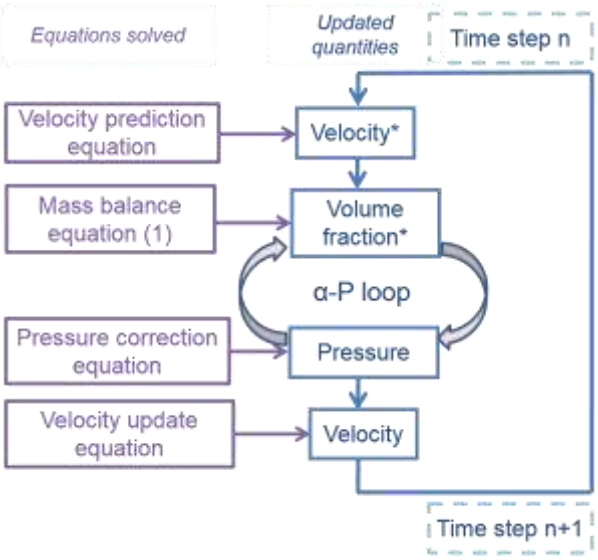


Figure 4. Schematic view of the numerical scheme of the CFD tool without the interface sharpening equation, * denotes the intermediate values.

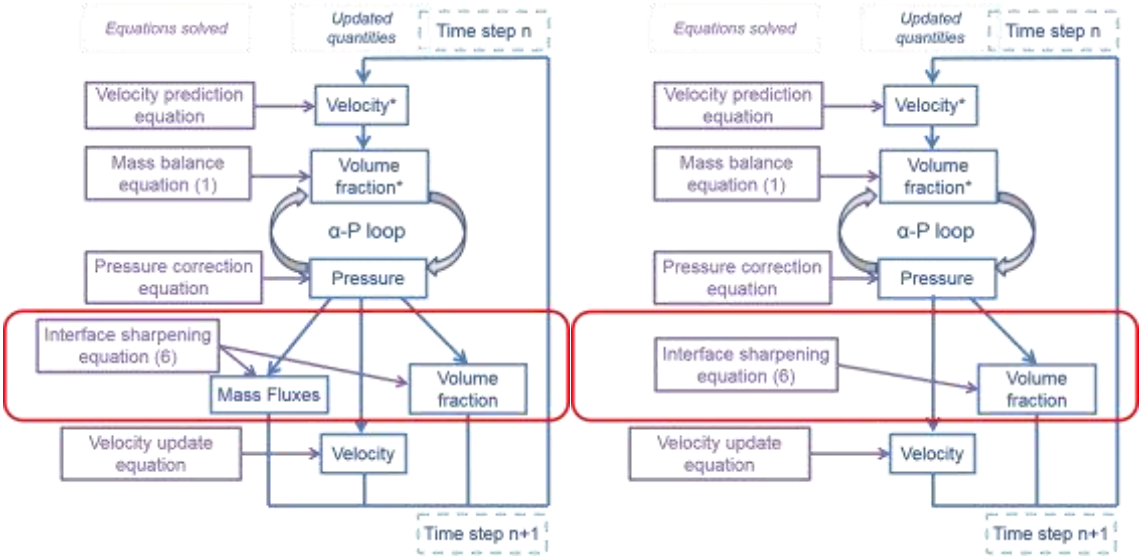
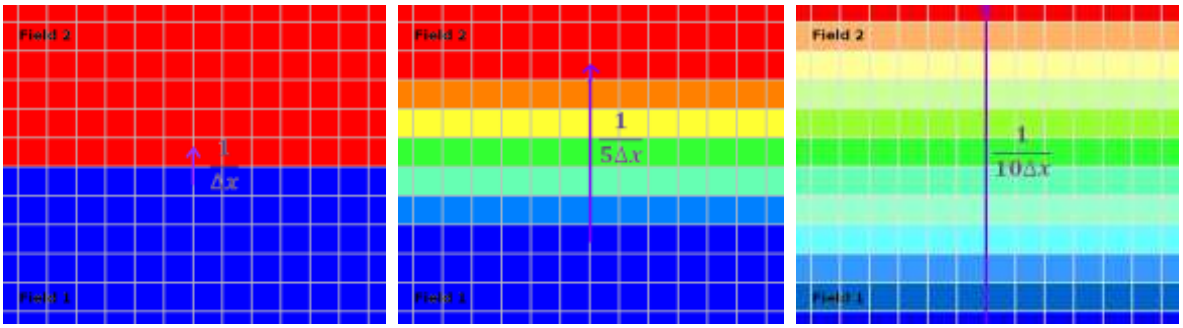


Figure 5. Schematic view of the numerical scheme of the CFD tool, left: conservative implementation of the interface sharpening equation, right: non conservative implementation, * denotes the intermediate values.



(a) **(b)** **(c)**

Figure 6. Schematic view of different state of interface smearing, the color scale represents the volume fraction of field 1, red corresponds to $\alpha_1 = 0$ and dark blue to $\alpha_1 = 1$, (a) sharp interface, not spread over few cells, (b) interface with a 5 cells thickness, (c) diffused interface with a 10 cells thickness, the purple arrow displays the volume fraction gradient over the interface.

Table 1

Properties of liquid water and air for the stationary bubble test case

Field	ρ (kg.m^{-3})	μ (Pa.s)
Water	1000	1.10^{-3}
Air	1.29	1.10^{-5}

Table 2

Effect of the conservative and non conservative implementation of the interface sharpening equation on the mass balance error obtained by time step in the whole domain and the intensity of the spurious velocities after 1s for the stationary bubble test case

Implementation	Mass balance error	max(u_g) (m.s^{-1})
Conservative	10^{-17} %	0.17
Non conservative	10^{-10} %	0.14

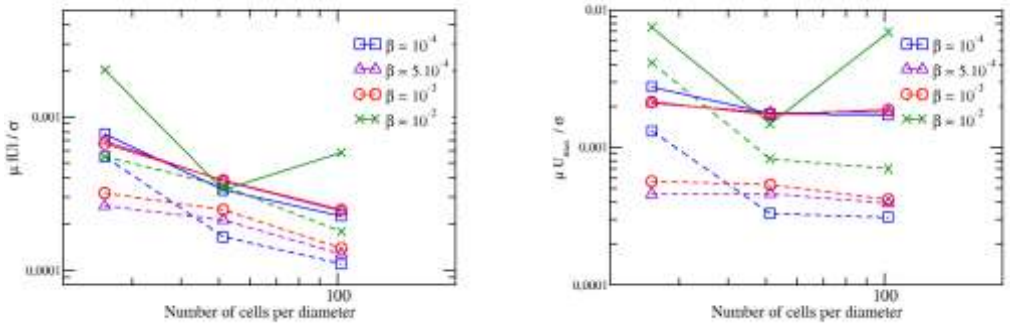


Figure 7. Capillary number according to the mesh refinement and the threshold value β, left: average velocity, right: maximum velocity, the solid lines correspond to the velocities evaluated according to Equation (17) and the dashed lines to Equation (18).

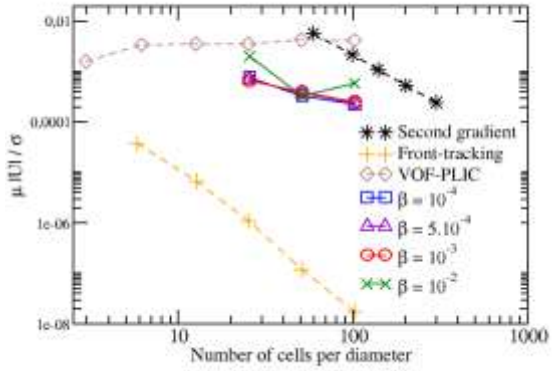


Figure 8. Capillary number according to the mesh refinement obtained with three different methods: the second gradient theory proposed by Jamet *et al.* [2000], the front tracking method of Popinet and Zaleski [1999], which includes a correction of the pressure gradient and the VOF-PLIC method [Li 1995].

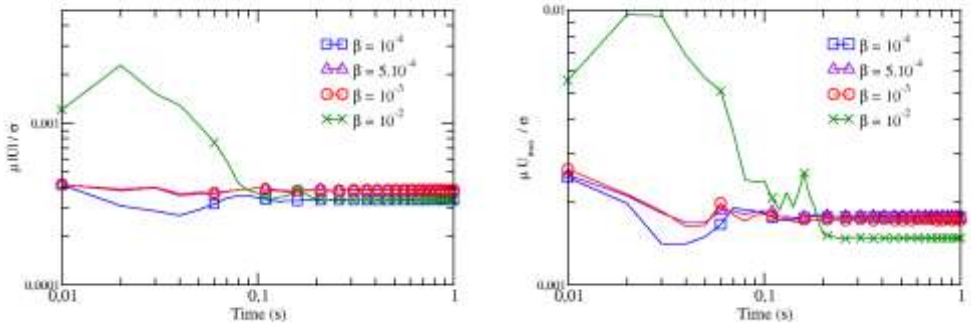


Figure 9. Capillary number over time according to the threshold value β, mesh with 128 x 128 cells, left: average velocity, right: maximum velocity, the velocities are evaluated in the whole domain $u = u_g$.

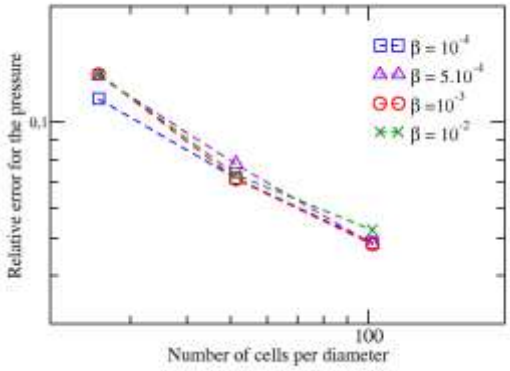


Figure 10. Relative error for the pressure according to the mesh refinement and the threshold value β obtained with the simulation of a stationary bubble.

Table 3

Properties of liquid and air for the test case of the oscillating bubble

Field	ρ (kg.m^{-3})	μ (Pa.s)
Liquid	7000	4.10^{-2}
Air	1.17683	$1.85.10^{-5}$

Table 4

Time steps according to the mesh refinement and the implementation of the interface sharpening equation for the oscillating bubble test case

Implementation of the interface sharpening equation	128 x 128 cells	256 x 256 cells
Conservative	5.10^{-4} s	$2.5.10^{-4}$ s
Non conservative	5.10^{-5} s	$2.5.10^{-5}$ s

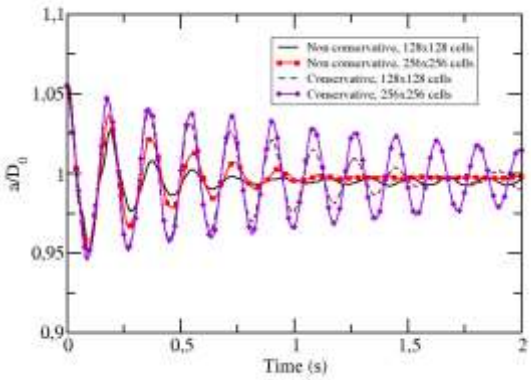


Figure 11. Evolution of the major axis a of the oscillating bubble normalized by the final bubble diameter D_0 over time for two mesh refinements and the conservative and non conservative implementation of the interface sharpening equation.

Table 5

Frequency ω_0 and characteristic time of decay τ_0 of the bubble oscillations according to the mesh refinement and the conservative implementation for an initial deformation rate of 0.05, the corresponding relative errors are given in brackets and the results of Caltagirone *et al.* [2011] in square brackets

Mesh refinement	128 x 128 cells		256 x 256 cells	
Implementation	Conservative	Non conservative	Conservative	Non conservative
ω_0 (s^{-1})	5.56 (2.6%) [4.95]	5.56 (2.6%)	5.68 (0.5%) [4.99]	5.56 (2.6%)
τ_0 (s)	0.56 (87%)	0.17 (96%)	1.82 (58%)	0.31 (93%)

Table 6

Iteration number of the interface sharpening equation according to the mesh refinement and the choice of the threshold value β

Mesh refinement	$\beta = 1.10^{-4}$	$\beta = 5.10^{-4}$	$\beta = 1.10^{-3}$	$\beta = 1.10^{-2}$
64 x 64 cells	25	4	2	1
128 x 128 cells	10	3	2	1
256 x 256 cells	7	2	1	1

Table 7

Bubble oscillation frequency according to the mesh refinement and the choice of the threshold value β, the relative errors are given in brackets

Mesh refinement	$\beta = 1.10^{-4}$	$\beta = 5.10^{-4}$	$\beta = 1.10^{-3}$	$\beta = 1.10^{-2}$
64 x 64 cells	-	5.1 s^{-1} (11%)	5.1 s^{-1} (11%)	5.2 s^{-1} (8.8%)
128 x 128 cells	-	5.6 s^{-1} (1.8%)	5.6 s^{-1} (1.8%)	5.5 s^{-1} (3.5%)
256 x 256 cells	5.6 s^{-1} (1.8%)	5.6 s^{-1} (1.8%)	5.6 s^{-1} (1.8%)	5.6 s^{-1} (1.8%)

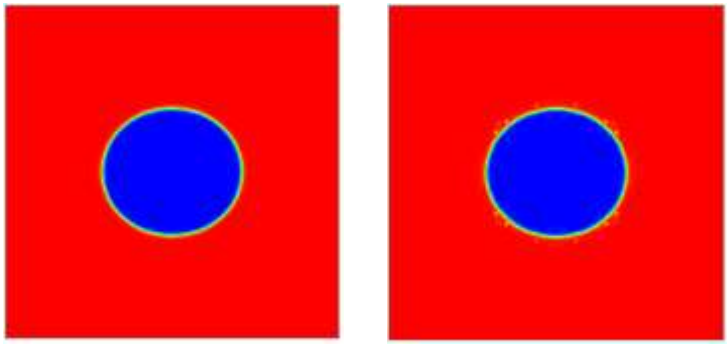


Figure 12. Oscillating air bubble in liquid at t = 0.01 s, mesh with 256 x 256 cells, left: $\beta = 1.10^{-3}$, right: $\beta = 1.10^{-2}$.

Table 8

Iteration number and bubble oscillation frequency according to the time step, $\beta = 1.10^{-3}$, the relative errors are given in brackets, mesh with the 128 x 128 cells

Time step	Iteration number	Oscillation frequency
0.025 ms	2	5.6 s^{-1} (1.8%)
0.0125 ms	1	5.7 s^{-1} (0.2%)
0.01 ms	1	5.7s^{-1} (0.2%)

Table 9

Properties of the two cases simulated in the Bhaga's rising bubbles test case

Simulation case	Re	μ_l (Pa.s)
Case b	3.57	2.02
Case d	13.3	0.77

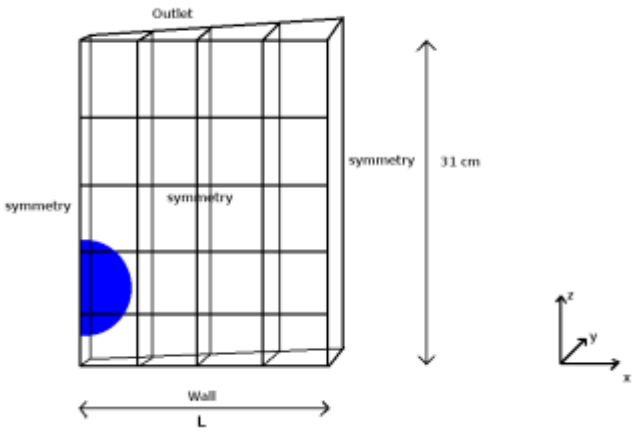
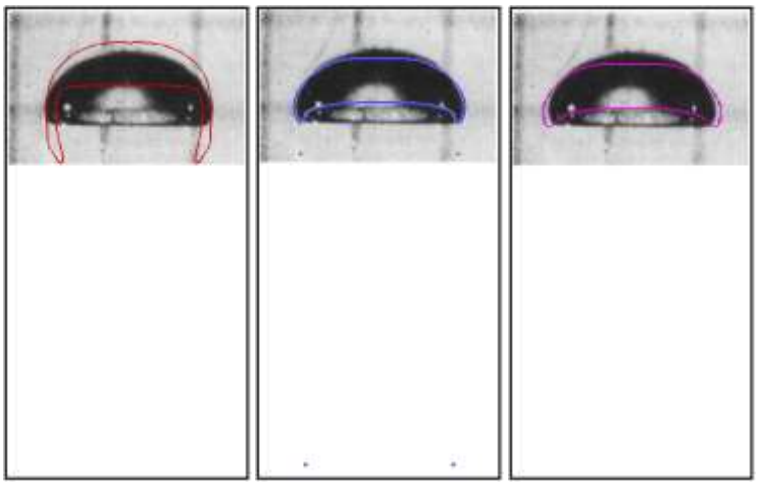


Figure 13. Schematic view of the mesh used for the simulation of the Bhaga's bubbles [Bhaga and Weber 1981], L = 10.38 cm for case b and L = 10.33 cm for case d.



(a) **(b)** **(c)**

Figure 14. Comparison of the simulated bubble shape in case d with the Bhaga's experimental observations [Bhaga and Weber 1981], (a) $\beta = 5.10^{-3}$, (b) $\beta = 1.10^{-3}$ and (c) $\beta = 5.10^{-4}$, the middle part of the domain is shown to highlight the creation of four small bubbles caused by the fragmentation of the large bubble for $\beta = 1.10^{-3}$.

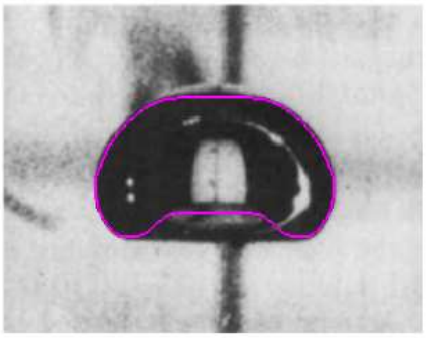


Figure 15. Comparison of the simulated bubble shape with the Bhaga's experimental observations [Bhaga and Weber 1981], case b, $\beta = 5.10^{-4}$.

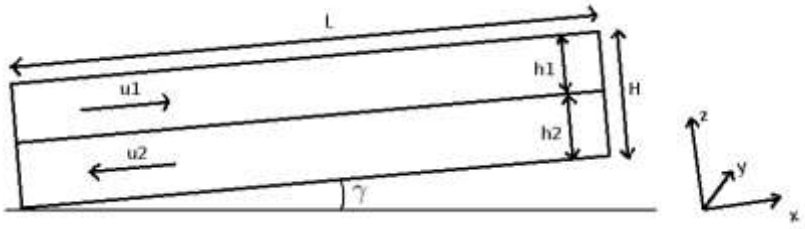


Figure 16. Schematic view of the Thorpe's experiment at initial conditions [Thorpe 1969].

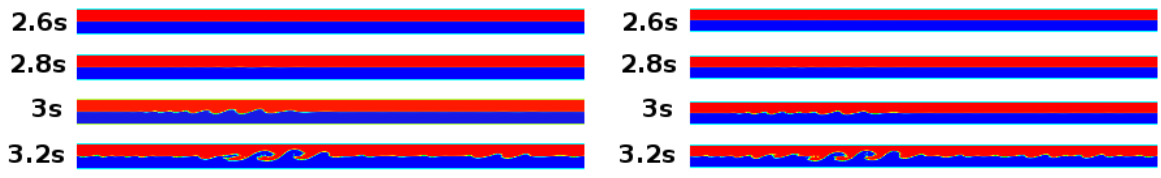


Figure 17. Influence of the interface smearing criterion in terms of interface shape, left: no interface smearing criterion, right: with the interface smearing criterion, mesh with 80 x 4880 cells, constant time step equal to 0.5 ms, only the middle 0.6 meters long section of the channel is shown.

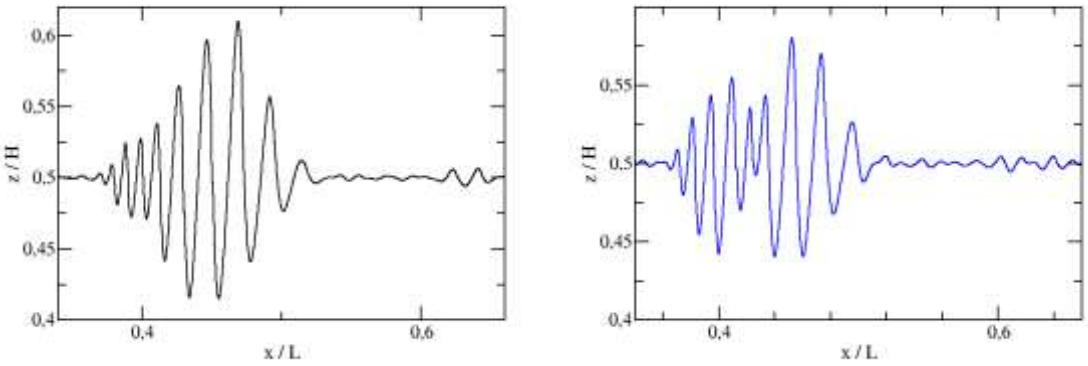


Figure 18. Physical location of the interface at 3 s, left: no interface smearing criterion, right: with the interface smearing criterion, only the middle 0.6 meters long section of the channel is shown, this representation is used to evaluate the wavenumber.

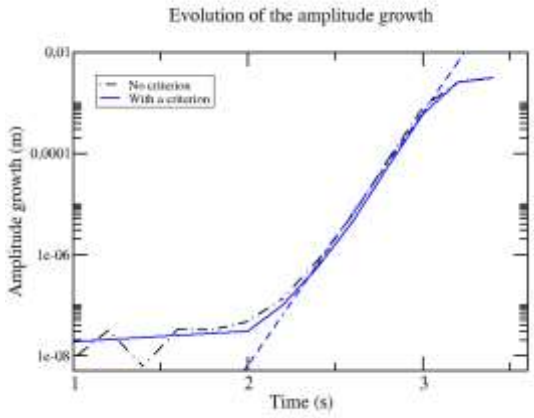


Figure 19. Amplitude growth obtained by evaluating the standard deviation of the interface over time, only the middle 0.6 meters long section of the channel is used for this analysis, the dashed line corresponds to the asymptotic amplitude growth used to determine the time of the instability onset.

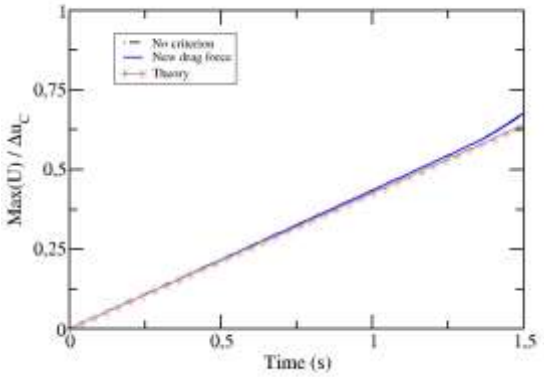


Figure 20. Average interface velocity U normalized by the critical velocity over time with and without the interface smearing criterion, U is defined in Equation (35), the theory is given by Equation (34), the three curves are superimposed.

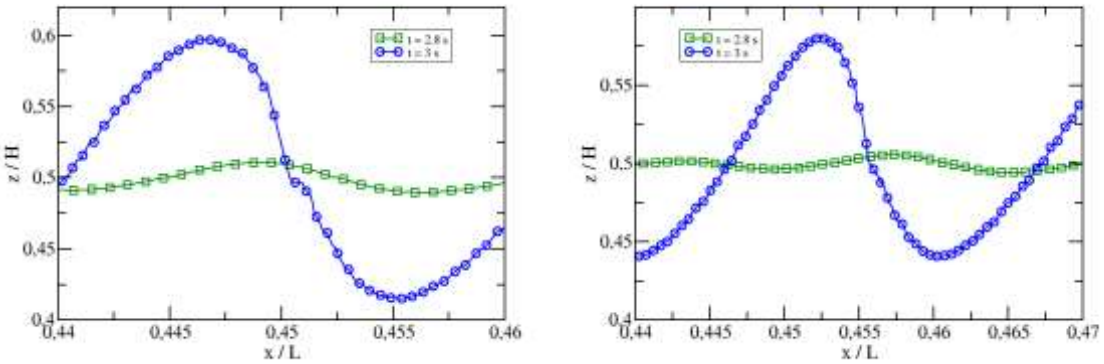


Figure 21. Physical location of the interface at different times for the evaluation of the wave speed, left: no interface smearing criterion, right: with the interface smearing criterion.

Table 10

Comparison of the critical wavenumber k_c, the time of the instability onset t_{onset} and the wave speed u_{waves} for the Kelvin-Helmholtz instabilities in the Thorpe's experiment configuration obtained in our simulations and in the simulations of Bartosiewicz *et al.* [2008] and Štrubelj [2009] according to the experimental and theoretical data

Results		k_c (m^{-1})	t_{onset} (s)	u_{waves} ($cm.s^{-1}$)
Threshold value	With/without the interface smearing criterion			
$\beta = 5.10^{-4}$	No criterion	202	2.1	1.6
$\beta = 5.10^{-4}$	With a criterion	219	2.1	3.1
$\beta = 1.10^{-3}$	With a criterion	200	2.1	1.9
Theory		232	1.5 – 1.7	2.38
Experiments [Thorpe 1969]		197 ± 58	1.88 ± 0.07	2.6
Bartosiewicz *et al.* [2008]		143	1.9	2.5
Štrubelj [2009]		157	2.0	3.0

Table 11

Summary of the test cases and parameters simulated in this article, the crosses symbolize that no reasonable results were obtained whereas the ticks correspond to an accurate simulation of the cases, the blue crosses and blue ticks refer to simulations, which have not be shown in this article

Implementation	Threshold value	Activation of the interface smearing criterion	Test cases			
			Oscillating bubble	Stationary bubble	Bhaga's bubble	Thorpe's experiment
Non conservative	$\beta = 5.10^{-4}$	Yes	X			
Conservative	$\beta = 1.10^{-2}$	Yes	X	X		
	$\beta = 5.10^{-3}$				X	
	$\beta = 1.10^{-3}$	Yes	✓	✓	X	X
	$\beta = 5.10^{-4}$	Yes	✓	✓	✓	✓
		No				X
	$\beta = 1.10^{-4}$	Yes	X	✓		